SEBASTIAN KORNET[a,b], DANIEL SŁAWIŃSKI[a], PAWEŁ ZIÓŁKOWSKI[a1]
and JANUSZ BADUR[a]

Analysis of unsteady flow forces on the thermowell of steam temperature sensor

[a] *Energy Conversion Department, The Szewalski Institute of Fluid-Flow Machinery of the Polish Academy of Sciences, Fiszera 14, 80-231 Gdańsk, Poland*

[b] *Conjoint Doctoral School at the Faculty of Mechanical Engineering, Gdańsk University of Technology, Narutowicza 11/12, 80-233 Gdańsk, Poland*

Abstract

In this paper, 3D numerical analysis of unsteady flow forces acting on the thermowell of steam temperature sensor is presented. According to that purpose, the CFD+CSD (computational fluid–solid dynamics) approach has been used. The nonstationary of fluid acting on the thermowell such as: Strouhal frequency, amplitude of pressure, structure of vortex, peak of pressure, field of pressure, field of velocity, etc. are studied analytically and numerically. There have been examined two cases of flow with changing both temperature, pressure and mass flow rate (operating daily and night in the unit with capacity of 380 MWe). In accordance with the standards ASME PTC 19.3 TW-2010 the possibility of entry into resonance has been examined.

Keywords: Unsteady flow; Resonance; CFD modeling, CSD modeling

Nomenclature

A – amplitude
a – characteristic dimension
$\mathbf{B}$ – linear strain-displacement transformations matrices

---

[1]Corresponding author. Email adress: pziolkowski@imp.gda.pl

$\mathbf{B_{NL}}$ –   nonlinear strain-displacement transformations matrices
$\mathbf{b}$ –   mass force of Earth gravity
C_{La} –   geometry constant
$\mathbf{D}$ –   material properties matrix
E –   Young's modulus and empirical constant $E = 9.81$
e –   internal and kinetic energy, $e = u + \frac{\mathbf{v}^2}{2}$
f –   frequency
$\mathbf{f}_N$ –   Navier friction force
$\mathbf{I}$ –   until tensor
$\mathbf{I_d}$ –   invariant of the deformation rate
$\mathrm{II_d}$ –   second invariant of the deformation rate
$\mathbf{J}_k, \mathbf{J}_\varepsilon$ –   diffusive flux of k and diffusive flux of ε
$\mathbf{K}$ –   linear stiffness matrix
$\mathbf{K^{NL}}$ –   nonlinear stiffness matrix
$\mathbf{K^R}$ –   stiffness matrix after local crossing yield stress
k –   turbulent kinetic energy, volume turbulent viscosity
l –   length
$\mathbf{M}$ –   mass matrix
$\dot{m}$ –   mass flow rate
Na –   Navier number
V –   volume
v –   steady ambient velocity of the uniform flow
$\mathbf{v}$ –   velocity, $\mathbf{v} = v_i \mathbf{e}_i$
p –   pressure
$\mathbf{q}$ –   heat flux, displacement matrix
r –   distance from the flow center
Re –   Reynolds number
S_k, S_ε –   sources of k and ε
Sh –   Strouhal number
T –   temperature
t –   period of the phenomena, time
$\mathbf{T}$ –   matrix of coordinates
$\mathbf{t}^{tur}$ –   turbulent momentum flux
U –   nondimensional velocity
y –   distance from the wall

Greek symbols

α –   thermal expansion
ε –   turbulent dissipation energy, the eddy viscosity
μ –   dynamic viscosity
κ –   von Kármán constatnt
$\boldsymbol{\sigma}$ –   elastic stress tensor
σ_{HMH} –   equivalent tensile stress
τ_w –   wall stress
ρ –   density
ν –   external viscosity, Poissone coefficient
λ –   thermal conductivity

Subscripts and superscript

0	–	coefficients of surface friction
2	–	second surface friction
I_d	–	invariant
B	–	the Boussinesq eddy viscicoty
e	–	machine element
i	–	in-line
lam	–	laminar
P	–	turbulent kinetic energy at point P or distance of the point P from the wall
res	–	residual
s	–	slip
T	–	turbulent
t	–	transversal
T	–	transposition
tur	–	turbulent
w	–	wall

1   Introduction

From the scientific and technical point of view, nonstationary flow force, operating on solid, are very important issue. In order to specify the similarity between periodical phenomena and to the case of nonstationary flows as well, there is entered the Strouhal number, Sh[1], which is the similarity number defined as [20]

$$\text{Sh} = \frac{a}{vt} = \frac{a\,f}{v}\,, \tag{1}$$

where a – is the characteristic dimension, v – steady ambient velocity of the uniform flow, t – the period of tested phenomena, f – frequency of the phenomena.

It should be added, that the Strouhal number, Sh, is used in the engineering technology to analysis of, e.g., flow around the vibrating body (aerofoil, the rod, thermowell), flow through a blade ring seated in the rotor disc, flow around a rotating propeller or screw propeller, etc.

Many of the literature items discuss the problem of the formation of vortices, changes in their structure, the impact of vortex structures on objects, on which they form. The research on the vorticity and the formation of structures at flow has been carried out for hundreds years, what is evidenced by sketches of Leonardo da Vinci [18, 19]. Great importance in the development of knowledge of periodical phenomena was works of von Kármán about vortices generation and works of Strouhal about frequency of

---

[1]Another name are Str, S, Ho

their formation. The exact description of these issues can be found in the works of the pioneers [21–23] and of contemporary authors [20,24]. Most of the published articles, relating to the nonstationary structures in flow, concerns the experimental work and analysis [3,7–9,17] while the importance of numerical works is growing [5,7,9,18].

The fundamental work in this regard is the analysis of the formation and development of vortex structures about flown around obstacles. A significant number of studies in this field concerns laminar-turbulent transition in the area, where unrecognized and not well recognized phenomena in single theory occurs. There are known works, in which the obstacle is the sphere [15,16], rotating sphere [6], trapeze [3], cube [4], the disk [25].

Especially important is the problem of vortices forcing vibrations, and vice versa – the vibration of devices or element of devices, affecting on changes in the vortex structure. In the last decade, numerous works concerning interaction of fluid and structures arrising in it on the solid have appeared [7,9,10]. It has resulted in creation a new norm for ASME PTC 19.3 TW-2010. Its requirements are implemented by producers of elements, particularly exposed to the interaction of fluid with solid body [2]. In this case, the similarity criterion is the frequency of the force, which can be directly compared with the free vibration frequency of the device, so we could determine whether the resonance occurs. An important tool in the analysis of this phenomenon is the combination of CFD + CSD (computational fluid dynamics + computational solid dynamics), increasingly called FSI – fluid solid interaction or fluid structure interaction.

Many studies have been carried out in area of the momentum FSI, for example, Jiang *et al.* [11] presented on a full-scale structural simulation of flow-induced mechanical vibrations and noise in a 5-stage centrifugal pump. They developed a data-interface tool to enable mesh matching and data transfer between the fluid and structure meshes. The vibration of the pump structure was simulated using a parallel explicit dynamic CSD code. This provided a time series of pressure fluctuations on the internal surface as force-boundary conditions. This study shows that it is feasible to use fluid-structure weakly coupled simulations to estimate the flow-induced noise generated in turbomachinery.

In the paper of Thapa *et al.* [12], computational fluid dynamics (CFD) and fluid structure interaction (FSI) were used to compare erosion in Francis runner blades with different design cases. Parametric survey was carried out to evaluate the relative effect of each design parameter on sediment

erosion. Several optimized designs were developed and analyzed with CFD tools to fulfill the desired condition of minimum erosion and maximum efficiency.

In [13], the flow past rigid-fixed and self-oscillating cylinders were studied at Re = 5000. For a rigid-fixed cylinder, CFD calculations were performed using the monitoring mesh technique. Extensive studies were conducted including mesh convergence study, time-step study, spanwise correlations and spectral calculations. For a self-oscillating cylinder, that had a span-length of 2D (two-dimensional), the numerical approach based on a fixed-point iteration, is used to predict drag vs. vibration amplitude and vibration amplitude vs. reduced damping.

Recently, Deng *et al.* [14] simulated using a finite volume based CFD code the steady high speed oil flow in the spool valve and the local temperature distributions around the notches. The temperature increase was due to the viscous heating effect, which is generally significant in highly-viscous fluid flow. Moreover, the deformation of the spool was simulated by the commercial code (a finite element based software). These two codes were simply coupled on the spool surface, where the temperature distributions, obtained from the CFD results, were imposed as the boundary conditions of the deformation calculations. It should be noted that this fluid-structure interaction (FSI) was modeled based on a loosely-coupled strategy, where the CSD code was started when the flow converges to a steady state and a stable thermal distribution had been reached. The aim of this study was to evaluate two different valve spools of the damage from jamming. Results had presented qualitative exhibitions of the temperature contours, appearances of the deformed spools, as well as the quantitative measurements of the radial deformations.

The main aim of the paper is to refer to the standards of ASME PTC 19.3 TW-2010 [2] for design thermowell of steam temperature sensor. We should add that a large number of experimental and numerical studies [3–18] of the wake behind the obstacles and vortex induced vibration has been performed. The boundary conditions of two different models have been considered – the standard wall function and the boundary condition with slip velocity. In accordance with the standards ASME PTC 19.3 TW-2010 the thermowell's possibility of entry into resonance has been examined. According to that purpose, the CFD+CSD (computaional fluid–solid dynamic) approach has been used.

2 Model description

2.1 The set of CFD balance equations

The five balance equations (that consist of one mass balance equation, three momentum balance equations and one energy balance equation) and two evolution equations for parameters defining turbulence (equation for turbulent kinetic energy evolution k and equation for turbulence dissipation evolution ε) have been described in Badur publications [1, 31]. A general formulation of balance equation was used in so-called nonindexed notation which denotes vector, $\mathbf{v} = v_i \mathbf{e}_i$, and tensors: $\mathbf{t} = t_{ij}\mathbf{e}_i \otimes \mathbf{e}_j$. Dyadic found is denoted as $\mathbf{v} \otimes \mathbf{v}$ [28]. So to maximize the use of the easily implementable matrix calculus, the starting point for CFD computation is to formulate universal set of mass, momentum and energy balance equations for the fluid, completed with equations for turbulence evolution k-ε in the form of

$$
\frac{\partial}{\partial t}
\left\{
\begin{array}{c}
\rho \\
\rho\mathbf{v} \\
\rho e \\
\rho k \\
\rho\varepsilon
\end{array}
\right\}
+ \mathrm{div}
\left\{
\begin{array}{c}
\rho\mathbf{v} \\
(\rho\mathbf{v} \otimes \mathbf{v}) + p\mathbf{I} \\
(\rho e + p)\mathbf{v} \\
\rho\mathbf{v}k \\
\rho\mathbf{v}\varepsilon
\end{array}
\right\}
= \mathrm{div}
\left\{
\begin{array}{c}
0 \\
\mathbf{t}^{res} \\
\mathbf{t}^{res}\mathbf{v} + \mathbf{q} \\
\mathbf{J}_k \\
\mathbf{J}_\varepsilon
\end{array}
\right\}
+
\left\{
\begin{array}{c}
0 \\
\rho\mathbf{b} \\
\rho S_e \\
\rho S_k \\
\rho S_\varepsilon
\end{array}
\right\},
\tag{2}
$$

where:

ρ –   fluid density $\rho = \rho(\mathbf{x}, t)$ generally dependent on time t and location $\mathbf{x}$;

$\mathbf{v}$ –   fluid velocity, $\mathbf{v} = v_i\mathbf{e}_i$;

p –   thermodynamical pressure,

$\mathbf{I}$ –   unity tensory, $\mathbf{I} = \delta_{ij}\mathbf{e}_i \otimes \mathbf{e}_j$;

$\mathbf{t}^{res}$ –   stress flux components, laminar and turbulent respectively, $\mathbf{t}^{res} = \mathbf{t}^{lam} + \mathbf{t}^{tur}$;

$\mathbf{b}$ –   mass force of Earth gravity,

e –   sum of internal and kinetic energy, $e = u + \frac{\mathbf{v}^2}{2}$;

$\mathbf{q}$ –   heat flux;

$\mathbf{J}_k, \mathbf{J}_\varepsilon$ –   diffusive flux of k and diffusive flux of ε with sources S_k, S_ε (various definitions of different authors exist in literature).

For each finite volume of the computational grid seven equations are solved (one for mass, energy, k and ε transport balance equation and three momentum balance equations).

2.1.1 Molecular flux of momentum

The fundamental momentum flux due to molecular viscosity is called viscous stress tensor and defined by Navier-Stokes constitutive equation [20]:

$$\mathbf{t}^{lam} = 2\mu\mathbf{d} - \frac{2}{3}\mu\mathbf{I_d}\mathbf{I}\,, \; \mathbf{d} = \frac{1}{2}(\mathrm{grad}\mathbf{v} + \mathrm{grad}^{\mathrm{T}}\mathbf{v})\,, \tag{3}$$

where dynamic viscosity μ is the only one constant of material.

2.1.2 Turbulent flux of momentum

Turbulent momentum flux, also called the Reynolds stress tensor is defined in an analogical form [29]:

$$\mathbf{t}^{tur} = 2\mu_T\mathbf{d} - \frac{2}{3}(\rho k + \mu_T\mathbf{I_d})\mathbf{I}\,. \tag{4}$$

In the formula (4), μ_T and k play the role of turbulent viscosities (shear and volume, respectively). Turbulent viscosity coefficient μ_T is connected with fundamental turbulence parameters k-ε, according to the two scale Laudner-Spaling models [30], as below

$$\mu_T = C_{La}\rho k^2\varepsilon^{-1}\,, \tag{5}$$

where C_{La} is the constant which needs to be calibrated for specific type of geometry, independent of kind of fluid (air, steam).

2.1.3 Standard wall functions

The presence of walls has naturally influence on the flow of fluid. Within the fluid layer, located in direct vicinity of the wall (called the wall layer), significant gradient of velocity and temperature are found. Together with the increase of the turbulent kinetic energy, related to the Reynolds stress and large gradients of the mean fluid velocity, the flow becomes more turbulent.

One of the methods to model the wall layer is the use of a 'wall function', which omits calculations of the viscous sublayer where the influence of the viscosity is the greatest and only half-empirically approximates the

phenomena occurring between the wall and the fully turbulent layer. Standard functions, used in this paper, are based upon those given by Launder and Spalding [30]. According to the so-called 'anisotropic law of the wall', the nondimensional velocity U^* is defined as [29]

$$U^* = \kappa^{-1} \ln(Ey^*) \,. \tag{6}$$

In the formula (6) one can find von Kármán constant $\kappa = 0.42$ and an empirical constant $E = 9.81$, whereas the nondimensional velocity U^* and non-dimensional distance y^* can be expressed as

$$U^* = U_P C_{La}^{0.25} k_P^{0.5} \rho \tau_w^{-1} \,, \tag{7}$$

$$y^* = \rho C_{La}^{0.25} k_P^{0.5} y_P \mu^{-1} \,, \tag{8}$$

where:

U_P –   means fluid velocity at point P (indicates P at particular variables denote their values taken at the point P), in a distance y of point P from the wall; index w denotes wall and f – fluid),

k_P –   turbulent kinetic energy k at the point P,

y_P –   distance of the point P from the wall,

μ –   dynamical viscosity,

τ_w –   wall stress.

2.1.4   Nonstandard turbulent momentum flux

The main hypothesis concerning turbulence, applied frequently by numerous researchers, say simply that turbulence leads to enhancemed of friction forces. This is exactly the way of Boussinesq's reasoning explained in 1877 paper. He assumed that classical linear (laminar) models of friction forces should be enhanced by adding and/or replacing by nonlinear (turbulent) model of friction [43–44].

Going into turbulent flow, Boussinesq has proposed nonlinear friction forces: bulk and surface ones [43]. The surface friction force was prolongation of the Du Buat friction forces with parts of linear and square of slip velocity [26–27]:

$$\text{surface friction force}: \qquad \tau_w = \mathbf{f}_f = \nu_0 \mathbf{e}_s + \nu \mathbf{v}_s + \nu_2 \mathbf{v}_s^2 \mathbf{e}_s \,, \tag{9}$$

where: $\mathbf{e}_s = \mathbf{v}_s / |\mathbf{v}_s|$, the coefficients ν_0, ν, ν_2 of surface friction nominally should be a constant or dependent from, for instant, the wall roughness.

So force of isotropic friction is a composition of three parts: the adherence dry friction v_0, the Navier linear friction and the kinetic friction v_2. However, the most important is the Navier friction force $\mathbf{f}_N = v\mathbf{v}_s$ which is a parallel to the slip velocity $\mathbf{v}_s$. The coefficient ν is called the 'external viscosity' [26–27].
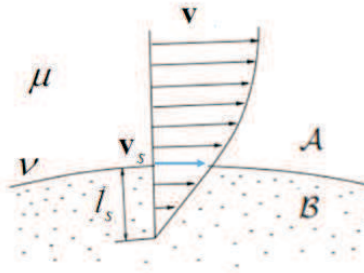

Figure 1: Definition of length slip and velocity slip for simple shear flow, according the Butcher concept of equivalent flows. Reconstruction from [26, 42].

The Boussinesq bulk friction force was based on a part with square gradient of velocity in a form proposed early by A.J. Dupuit in 1865 (Tab. 1). However in analogy to external friction the internal (bulk) friction force should been defined was [44]

$$\mathbf{t}^{res} = \mu_0\mathbf{I} + \mu\mathbf{d} + \mu_T\mathbf{d}^2\,, \tag{10}$$

where $\mu_0\mathbf{I}$ is the adherence part, μ – is the Navier linear or nonlinear dynamic viscosity and μ_T – turbulent viscosity. Concept models of 3D bulk flow resistance based on the eddy viscosity concept is presented in Tab. 1.

2.1.5 Nonstandard wall function – boundary condition

In contrast, in some special applications, for example, in microfluidic and nanofluidic devices, where the surface-to-volume ratio is huge, the slip velocity behaviour is more typical, and the slip hydrodynamic boundary condition is usually used. Regardless the slip physical mechanism, the degree of slip is normally quantified through the slip length.

Nonstandard wall function is dependent on slip length, l, which is also considered as Navier number, Na, (respectively) [26–27]:

$$l_s = \mu\nu^{-1}, \qquad \text{Na} = l_s a^{-1}\,. \tag{11}$$

Table 1: Models of 3D bulk flow resistance based on the eddy viscosity concept where r is a distance from the flow center, $\mathbf{v}_s$ – the velocity slip, y – a distance from the wall, p – pressure, n – constant, and $\varepsilon = \mu + \mu_T$ – the eddy viscosity [44].

$\mathbf{t}^{res} = \mathbf{t}^{lam} + \mathbf{t}^{tur} + \cdots$		
$\mathbf{t}^{res} = 2\varepsilon\mathbf{d}$	(Navier 1822,	$\varepsilon = const$)
$\mathbf{t} = 2\varepsilon\mathbf{d} + \varepsilon_P\sqrt{\mathrm{II_d}}\mathbf{I}$	(Poisson 1831,	$\varepsilon_P = const$)
$\mathbf{t}^{res} = \varepsilon_2\mathbf{d}^2$	(Darcy 1856,	$\varepsilon_2 = const$)
$\mathbf{t}^{res} = \varepsilon_1\mathbf{d} + \varepsilon_2\mathbf{d}^2 + \varepsilon_3\mathbf{d}^3 + \ldots$	(Dupuit 1848,	$\varepsilon_i - const$)
$\mathbf{t}^{res} = 2\varepsilon_L\mathbf{d}$	(Lévy 1858,	$\varepsilon_L = Au(r)\sqrt{r}$)
$\mathbf{t}^{res} = 2\varepsilon_{B_s}\mathbf{d}$	(Bresse 1868,	$\varepsilon_{B_s} = A^n p^n$)
$\mathbf{t}^{res} = 2\varepsilon_{B_s}\mathbf{d} + \varepsilon_2\nabla\mathbf{d} + \varepsilon_1\nabla\nabla\mathbf{d} + \ldots$	(Kleitz 1869,	$\varepsilon_1, \varepsilon_2 = const$)
$\mathbf{t}^{res} = 2\varepsilon(1 + l_{Levy}^2\nabla^2)\mathbf{d}$	(Lévy 1871,	$l_{Levy}^2 - mixing\,length$)
$\mathbf{t}^{res} = \varepsilon_B\mathbf{d}$	(Boussinesq 1877,	$\varepsilon_B = A_B\mathbf{v}_s^2 y$)
$\mathbf{t}^{res} = \varepsilon_{Br}\mathbf{d}$	(Briullion 1904,	$\varepsilon_{Br} = \varepsilon\left(p^n, \mathrm{I_d}, \mathrm{II_d}, \mathrm{III_d}\right)$)
$\mathbf{t}^{res} = \varepsilon_{Pr}\mathbf{d}$	(Prandtl 1914,	$\varepsilon_{Pr} = A\sqrt{\mathrm{II_d}}y$)
$\mathbf{t}^{res} = 2(\mu + \varepsilon_{La})\mathbf{d}$	(Laduner 1972,	$\varepsilon_{La} = \rho C_{La}k^2\varepsilon^{-1}$) – Eq. (5)

This last coefficient ν Eq. (11) depends from, both, a kind of fluid and a contacting solid. The characteristic dimension of a channel a usually is identified with a radius of tube.

Nonstandard wall function is connected with the boundary condition. So consistencies of boundary condition could be simply recognized if we compare the internal and external coefficients that appear in the model:

$$(f\mathbf{I} + 2\varepsilon_B(\mathrm{II_d}, |\mathbf{v}_s|)\mathbf{d} + \mu_2\mathbf{d}^2)\mathbf{n} = \nu_0\mathbf{e}_s + \nu\mathbf{v}_s + \nu_2\mathbf{v}_s^2\mathbf{e}_s \,. \tag{12}$$

This consistency could even be extended on reversible properties of the model, i.e., the internal (Euler) and the external (Stokes) pressures p and $\bar{\omega}$, respectively [26].

In Eq. (12) we have the Boussinesq eddy viscosity, ε_B, [43–44]

$$\varepsilon_B\big(\mathrm{II_d}, |\mathbf{v}_s|\big) = A_B\mathbf{v}_s^2 y \,, \tag{13}$$

$\varepsilon_B = A_B\mathbf{v}_s^2 y$ concept is a two scale concept, namely: 1) slip velocity $\mathbf{v}_s$ scale, 2) wall distance y scale. In opinion of authors, it is the most correct proposition of eddy viscosity. Actually, we are in the course of testing of the Boussinesq eddy viscosity concept, putting instead of exact slip velocity $\mathbf{v}_s$ so-called the wall shear velocity $\mathbf{v}_{sh} = \sqrt{\tau_w\rho^{-1}}\mathbf{s}$.

2.2 The set of CSD balance equations

The problem of natural vibration has been discussed in [32,36], modal vibration and harmonic analysis by used FEM (finite elements methods) type of discretization in [9–11,33,34,37,38,40]. The problem of determination of nonstationary load coming from steam flow, amplitudes of excitation loads for non-stationary flow and partial power turbine have recently been discussed in [11,37,38].

In analogy to CFD set of governing equations, the appropriate set of CSD governing equations is determined as follows [31]:

$$
\frac{\partial}{\partial t}
\left\{\begin{array}{c} 1 \\ \rho\mathbf{v} \\ \rho e \\ \rho\mathbf{e}^{pl} \\ \rho\boldsymbol{\alpha} \\ \rho r \end{array}\right\}
+ \mathrm{div}
\left\{\begin{array}{c} 0 \\ \rho\mathbf{v}\otimes\mathbf{v} \\ \rho e\mathbf{v} \\ \rho\mathbf{e}^{pl}\otimes\mathbf{v} \\ \rho\boldsymbol{\alpha}\otimes\mathbf{v} \\ \rho r\mathbf{v} \end{array}\right\}
= \mathrm{div}
\left\{\begin{array}{c} 0 \\ \boldsymbol{\sigma} \\ \boldsymbol{\sigma}\mathbf{v}+\mathbf{q} \\ 0 \\ 0 \\ \mathbf{J_r} \end{array}\right\}
+
\left\{\begin{array}{c} 0 \\ \rho\mathbf{b} \\ \rho S_e \\ \rho S_{pl} \\ \rho S_\alpha \\ \rho S_r \end{array}\right\} . \quad (14)
$$

Our analysis and calculations in solid body are based on three-dimensional (3D) modal and harmonic analysis typical for the CSD [31,37]. CSD is point-blank analogy CFD. Both methods use the same equations balance (mass, momentum and energy). Discretization method for the CSD and CFD is arbitrary (FEM, FVM, etc) but the governing equations are identical. This architecture solving equation greatly simplifies analyses FSI [11–13] and thermal–FSI [39]. Results of excitation frequency have been verified by results obtained in the CFD.

The stress and strain, calculated in CSD, will be saved by meaning of second principal invariant of stresses and strains. For the modal analysis the momentum balance received a form useful to a computational applications [31,37,40]:

$$
\mathbf{M\ddot{q}} + \left(\mathbf{K}(\boldsymbol{\sigma}) + \mathbf{K}^{NL} + \mathbf{K}^{R}\right)\mathbf{q} = \mathbf{F}^{\mathrm{ext}} , \quad (15)
$$

where 'dots' represent a time derivative and $\mathbf{M}$, $\mathbf{K}(\boldsymbol{\sigma})$, $\mathbf{K}^{NL}$, $\mathbf{K}^{R}$ are the mass matrix, linear stiffness matrix dependent on strength $\boldsymbol{\sigma}$, initial strain-displacement matrix (it is original definition of nonlinear initial displacement of thermowell), residual matrix (is original definition representing stiffness matrix after local crossing yields stress in the material thermowell), respectively [37], defined as follows:

$$\mathbf{M} = \iiint_{V_e} \mathbf{N}^T \rho \mathbf{N} dV \,, \tag{16}$$

$$\mathbf{K}(\boldsymbol{\sigma}) = \iiint_{V_e} (\mathbf{N}^T \mathbf{B}^T \mathbf{D} \mathbf{B}_{NL} \mathbf{N} + \mathbf{N}^T \mathbf{B}_{NL}^T \mathbf{D} \mathbf{B}_{NL} \mathbf{N} + \mathbf{N}^T \mathbf{B}_{NL}^T \mathbf{D} \mathbf{B} \mathbf{N}) dV \,, \tag{17}$$

$$\mathbf{K}^R = \iiint_{V_e} \mathbf{N}^T \mathbf{T}^T \begin{bmatrix} \sigma_{xx} & \sigma_{xy} & \sigma_{xz} \\ & \sigma_{yy} & \sigma_{yz} \\ sym & & \sigma_{zz} \end{bmatrix} \mathbf{T} \mathbf{N} dV \,. \tag{18}$$

Here V_e is the volume of machine element, $\mathbf{B}$, $\mathbf{B}_{NL}$ are the linear and nonlinear strain–displacement transformations matrices, $\mathbf{D}$ is the material properties matrix, $\mathbf{T}$ is matrix of coordinates and ρ is density of solid [37], for instant

$$\mathbf{B} = \begin{bmatrix} \partial_x & 0 & 0 \\ 0 & \partial_y & 0 \\ 0 & 0 & \partial_z \\ 0 & \partial_z & \partial_y \\ \partial_z & 0 & \partial_x \\ \partial_y & \partial_x & 0 \end{bmatrix} \,. \tag{19}$$

3   FSI analysis

In this study, one-way FSI analysis was conducted in order to define excitation, which are formed in the fluid as a result of flow around the thermowell. Then, the obtained results were used as data to determine the risk acting on the thermowell of steam temperature sensor. In the next subsection there are shown the boundary conditions and the results of the simulations of both CFD (only the standard wall function) and CSD analysis.

3.1   CFD analysis

3.1.1   CFD boundary conditions

Boundary conditions for CFD calculations are presented in Tab. 2. There were considered two cases of work of pipelines supplied control stage of turbine 380 MWe, so the power supply at reduced pressure and mass flow rate of steam – night work 180 MWe and daily work with the parameters of nominal 380 MWe. Previously described model was used. On the other hand, geometry of the thermowell and the pipeline are shown in Fig. 2.

Table 2: Boundary conditions assumed to calculations.

Parameter	Unit	Daily work	Night work
$\dot{m}$	kg/s	101	76
p	MPa	15.37	11.96
T	°C	535	520.7
N	MWe	380	180

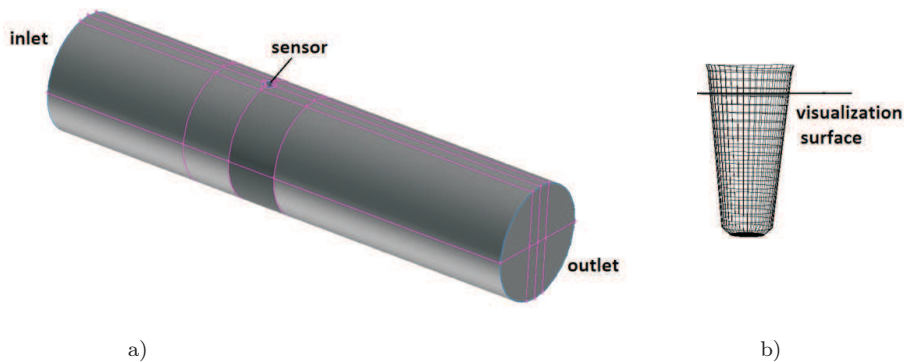a)   b)

Figure 2: a) Geometry of pipeline with marked location of the thermowell of thermometer (sensor), and b) geometry of the thermowell of steam temperature sensor with marked visualization of the results surface.

3.1.2 CFD analysis

As already mentioned, the analysis of air forces acting on the thermowell of steam thermometer M30 [37], mounted in pipeline supplied HP part of steam turbine, for two different cases – daily and night work, was performed. The quantitative results are shown in Tab. 3 and Fig. 3. In turn, Fig. 4 presents changes over time in static pressure difference in directions: the direction of the flow (in-line excitation) and perpendicular to the axis of the pipeline (transverse excitation), both for daily and night work. It should be added that drag pressure difference indicates in-line excitation and lift pressure difference causes transverse excitation (compare Fig.3 and Fig.4. with Tab. 3).

Basing on these results, it could be concluded that the amplitude of transverse excitation is about 10 times higher than the in-line excitation. Thus, these changes in the flow and force acting on the thermowell of ther-
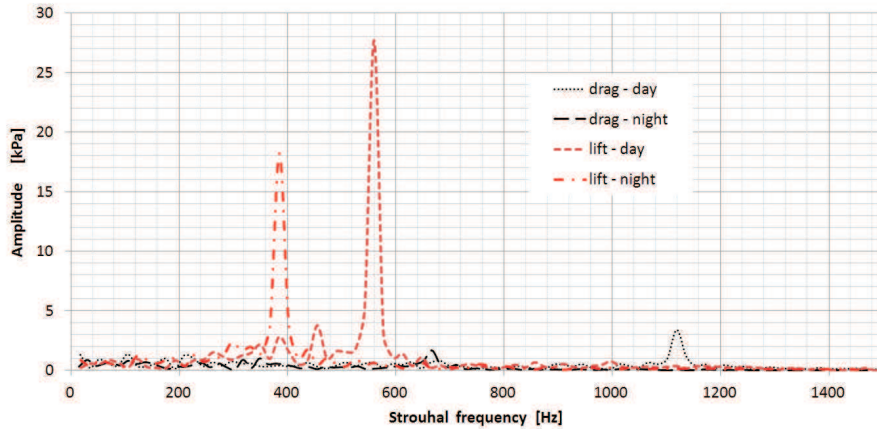
Figure 3: Spectral analysis by Fourier transform of timelines of the static pressure difference. Drag pressure difference indicates in-line excitation and lift pressure difference causes transverse excitation (compare Tab. 3).

Table 3: Frequencies and amplitudes of forces acting on the thermowell, where the index i applies to in-line excitation to the flow, and the index t to transverse excitation.

Parameter	Unit	Daily work	Night work
f_t	Hz	559	333
A_t	Pa	27700	18200
f_i	Hz	1119	667
A_i	Pa	3380	1670

mometer, are largely caused by lift force. The dominant excitation during the daily work is at a frequency $f_t = 559$ Hz and amplitude $A_t = 27700$ Pa, while during night work moves in the frequency range of $f_t = 333$ Hz and amplitude $A_t = 18200$ Pa.

Analyzing Fig. 4 it must be concluded, that in the case of force lift the size of the static pressure difference, depending on the time, took the shape of sinusoid, whose amplitude ranges from ± 40–35 kPa – at daily work and ± 25–15 kPa – at night work. Daytime work regime characterizes by larger and faster changes in the differential pressure acting on the thermowell. Basing on these results, the material, which thermowell of steam temperature sensor was made of, has been loaded in further analysis of CSD.

There was also analyzed the shape of vortex structures (Fig. 5) on the two sides of the geometry of the thermowell at the height of the sensor as
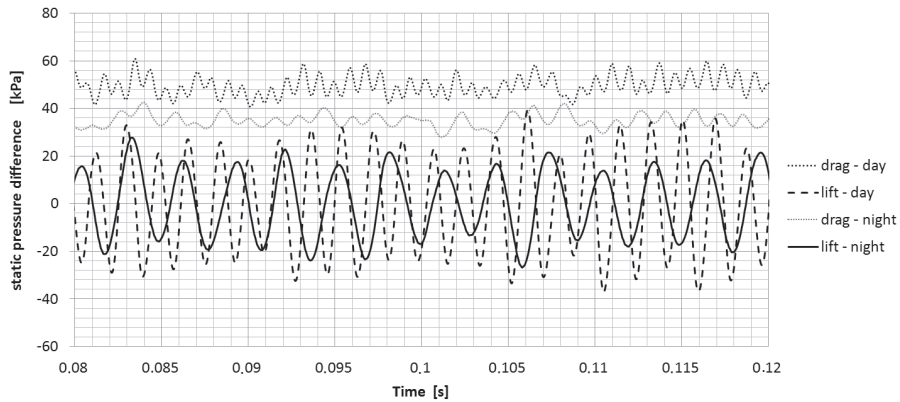
Figure 4: Diagram of static pressure difference in time. Drag pressure difference indicates in-line excitation and lift pressure difference causes transverse excitation.

shown in Fig. 2, in detachment of the low pressure area (Fig. 6). It should be noted, that larger vortices are formed in the area away from the end the thermowell of steam temperature sensor – closer to pipeline mantle in the regime of night work. At daily work regime, created vortices are entrained by the flow, where they disperse. While at regime of night work, created vortices break up about the walls of the pipeline.

Cross section of velocity flow has been presented in Fig. 7. Behind the thermowell, steam velocity is significantly lower than in front of it. Both, velocity and vorticity distribution of fields for the geometry of the thermowell of steam temperature sensor look like meanders on the river, which is the typical von Kármán vortex street. This is consistent with the results of many experiments [7] and already well established knowledge [20–24].

Basing on Figs. 5–7 it should be added, that larger vortices, but with lower frequency, are formed in the regime of night work, even if the velocities in flow are similar. It should also be noted that there is a much higher pressure in the pipeline of steam in a daily regime, so the flow is tighter and thus the potential for creating a vortex structures reduces.

In order to confirmation of the correctness of the results, the resultant points were marked on the diagram of the depending Reynolds number on Strouhal number (Fig. 8), taken from ASME norm [2]. The position of points in Fig. 8 should be considered as satisfactory, because they took place in the area defined experimentally. It is worth to mention, that the diagram with norms from ASME PTC 19.3 TW–2010 refers to the obstacles, found in the whole height of the channel with a uniform cross-section, and
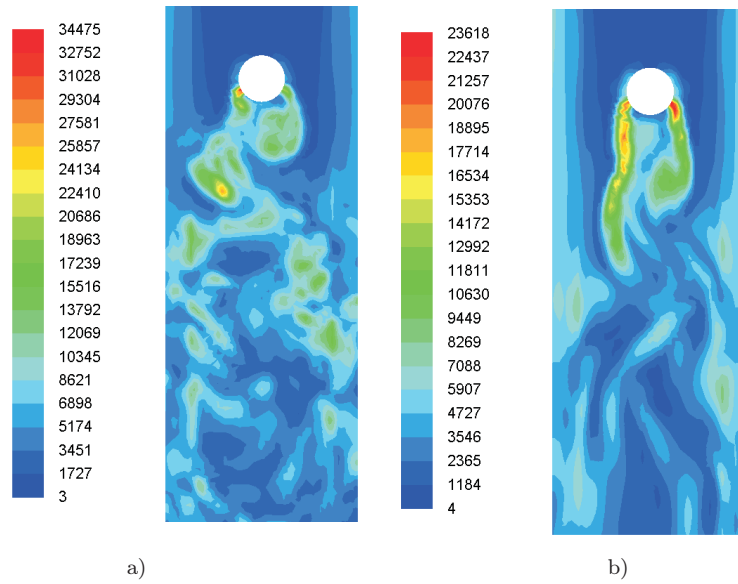
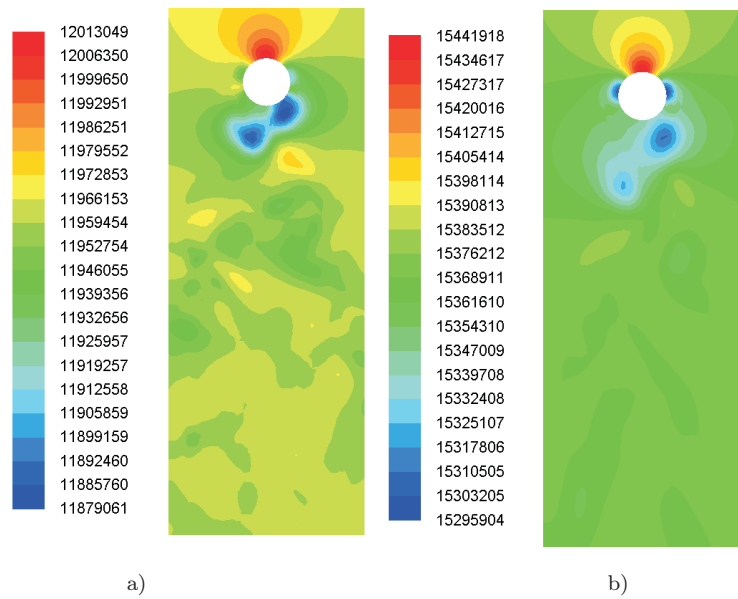Figure 5: Cross section of vorticity flow [1/s]: a) night work, b) day work.

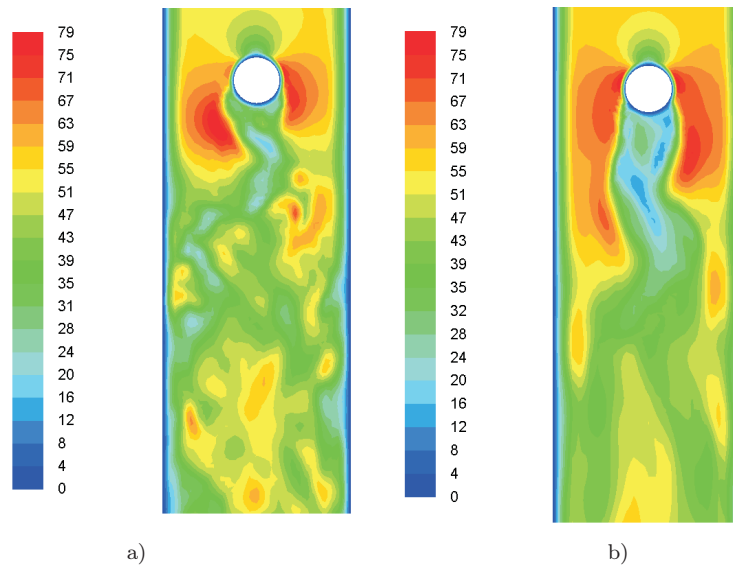Figure 6: Cross section of static pressure [Pa]: a) night work, b) day work.

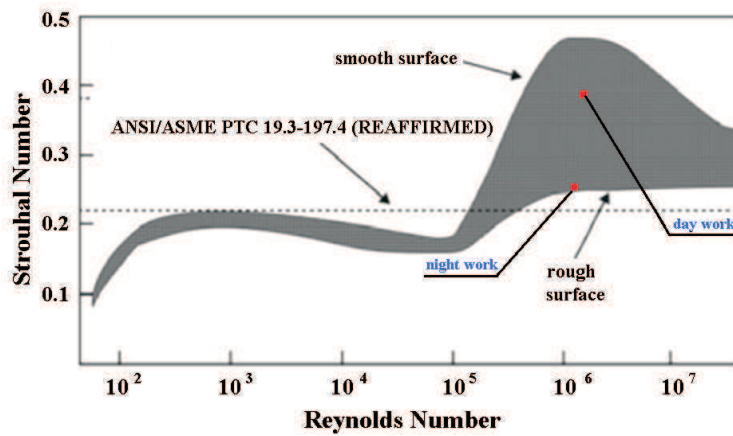Figure 7: Cross section of velocity flow [m/s]: a) night work, b) day work.

Figure 8: Comparison of St(Re) from ASME PTC 19.3 TW–2010 to numerical results.

in the case of this thermowells the flow was only partially obscured, and additionally the thermowell has the shape of a truncated cone.

3.2   CSD analysis

3.2.1   CSD boundary conditions

Figure 9 shows the geometry of the thermowell after making discretization which was used to calculate the frequency of free vibrations of the housing of steam temperature sensor. In the Fig. 9, there are marked places of application the aerodynamic loads, whose values were determined on the basis of above mentioned calculation of CFD.
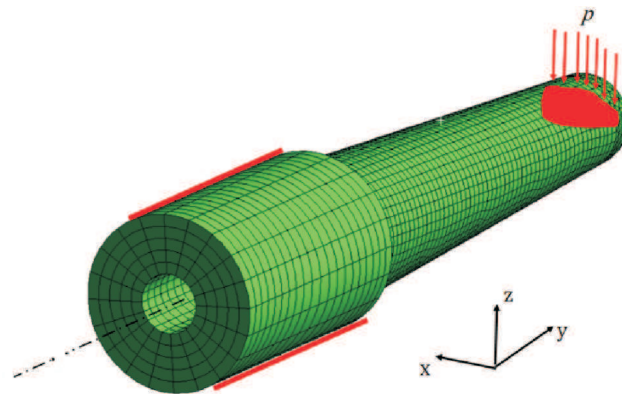

Figure 9: The housing of the thermowell after making discretization and with marked place of application of the boundary conditions.

The upper area, marked by arrows, is the place, where the highest pressure differences and most intense changes in the flow conditions were recognized. For these simulation, there was adopted most adverse load variant, which could be attributable to the boundary conditions describing the work at daily work regime. The highest pressure differences applicated in this situation was 1 MPa.

To mount a structure, 6 degrees of freedom was taken away from the area marked by lines (left side of Fig. 9). Place of geometry attachment corresponds to a screwed connection of housing with pipeline.

As the material of the thermowell was taken steel ST12 with the following mechanical properties in the temperature range from $T = 20$–600 [°C]:
$E = -8 \times 10^{-8}T^4 + 0.0005T^3 + 0.2656T^2 - 105.09T + 220583$ [MPa]
$v = - - 9 \times 10^{-14}T^4 + 1 \times 10^{-10}T^3 - 3 \times 10^{-8}T^2 + 5 \times 10^{-5}T + 0.2839$ [–]

$\alpha = -5 \times 10^{-18} T^4 + 4 \times 10^{-15} T^3 - 1 \times 10^{-12} T^2 + 4 \times 10^{-9} T + 1 \times 10^{-5}$ [1/K]

$\lambda = -5 \times 10^{-11} T^4 + 6 \times 10^{-3} T^3 - 2 \times 10^{-5} T^2 + 0.0074 T + 23.852$ [W/(mK)]

In these relationships T refers to degrees Celsius.

3.2.2   CSD results

Firstly, the equivalent tensile stress σ_{HMH} of thermowell, caused by maximum momentary load applied in the area of P, was calculated (effect of pressure on the other surface areas of the thermowell has been neglected). The designated equivalent tensile stress σ_{HMH} of thermowell in cross-section, shown in Fig. 2, are small, ranging from $\sigma_{HMH} = 2.1$ MPa on the outside, to $\boldsymbol{\sigma}_{HMH} = 0.6$ MPa inside the thermowell (cross-section in Fig. 10).

As shown in Fig. 10, the displacement trajectory corresponds to uniaxial bending. The greatest equivalent tensile stress was put in the place of the notch, connecting the conical part of the thermowell with the screwed part mounted in the housing of the pipeline and it is $\sigma_{HMH} = 3.7$ MPa. Its value is small, so in such a regime the thermowell could safely operate without the danger of significant loss of lifetime.
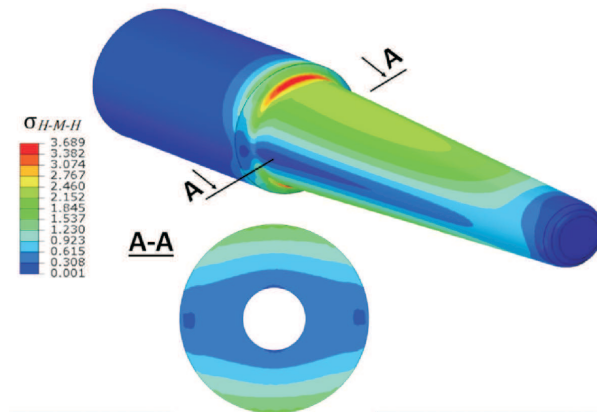

Figure 10: Fields of equivalent tensile stress σ_{HMH}, obtained on the surface and in cross-section of thermowell.

In Tab. 4 there has been shown calculated frequency of vibrations. Simulations were performed for the form of free and tight vibration, as a result of asymmetric aerodynamic excitations. Because the results has showed little

effect of the tight thermowell on change in its frequency of vibrations and its significant change under the influence of the changing temperature of the steam flowing around it, this table shows the results for different boundary conditions. With daily loads reaching values about 1 MPa, the differences in the frequency of free and tight vibrations were not noticeable.

Table 4: Frequency of vibrations of thermowell for different boundary conditions.

Mode	Tight Vibrations [Hz]	Free Vibrations [Hz]	Tempe-rature [°C]	Mode	Tight Vibrations [Hz]	Free Vibrations [Hz]	Tempe-rature [°C]
1	1986	1981.8	100	1	1629.8	1628	530
2	1989	1982.1	100	2	1630	1629	530
3	7585	7569.3	100	3	6233	6217.2	530
4	7585.3	7569.6	100	4	6134	6118.4	530
5(t)	11383	11361	100	5(t)	9278	9257	530

The first and second mode shape is characterized by line of nodes at the base of thermowell respectively in horizontal and vertical plane (1st lateral and vertical bending – Fig. 11a–b). The second and third form is characterized by two nodal line also in horizontal and vertical planes (Fig. 11c–d – 2nd lateral and vertical bending). The fifth is a form of torsional mode shape. As already mentioned, the size of excitation frequency was defined by detailed CFD simulation and is shown in Tab. 3. It should be noted that, if each of these characters was induced, it would be threat to lifetime of the thermowell and would certainly contribute to premature failure or destroy.

On Fig. 12 there has been presented, how the frequency of thermowell free vibrations changes while the temperature of elements increases. In result of increasing temperature, the coefficients, characterizing used material, change. While increasing temperature from 20 °C to 535 °C, the size of used Young's modulus value changes more than half. This change has its representation in the course of the curves presented in diagram. Assuming those material values as true, we could make conclusion, that during nominal work there is not resonant excitation in thermowell through any form of its free vibrations.
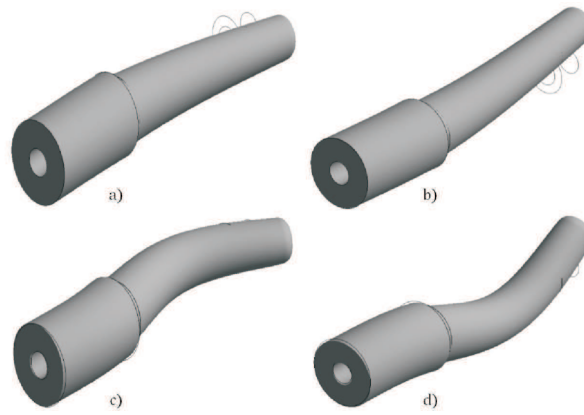
Figure 11: The mode shapes of thermowell : a) first, b) second, c) third, d) fourth.
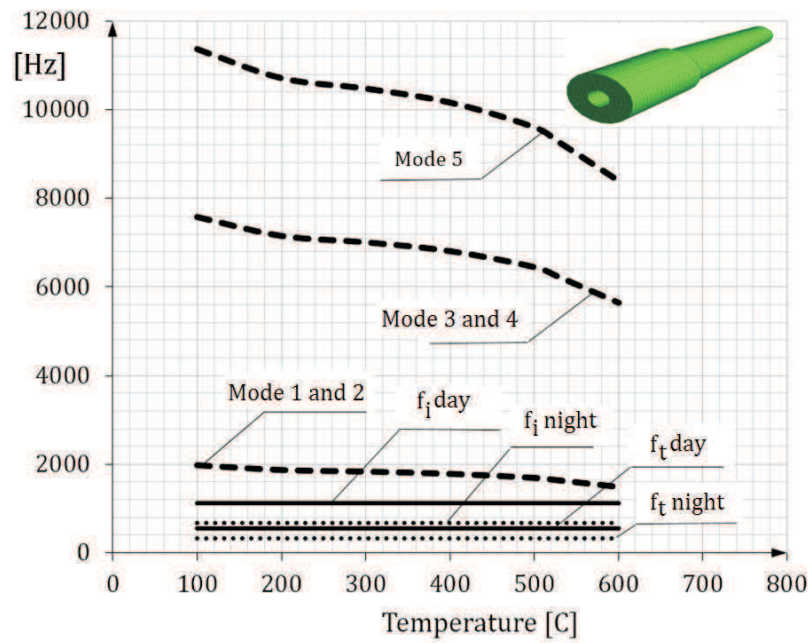

Figure 12: Change in frequency of free vibration while increasing temperature of thermowell.

4   Conclusions

One-way FSI analysis was carried out on the thermowell of steam thermometer and it was shown, that it does not find itself in a dangerous area of work. To this purpose, there was determined the flow excitation, and then the dynamic analysis of thermowell was performed. It was found different Strouhal frequency – excitation than free vibration of solid body. Therefore, the construction is offset and does not require two-way FSI analysis.

In addition, the nature of the flow was analyzed in detail. In order to confirmation of the correctness of the results, there were applied resultant points on the diagram of the relation between Strouhal and Reynolds number, taken from ASME PTC 19.3 TW–2010.

There are following conclusions from the CFD analysis:

- the dominant excitation during the daily work runs at a frequency $f_t = 559$ Hz and amplitude $A_t = 27.7$ kPa, while during night work moves to the frequency range of $f_t = 333$ Hz and amplitude $A_t = 18.2$ kPa;

- regime of daily work contributes to bigger and faster changes in the difference pressure acting on thermowell;

- larger, but with lower frequency, vortices are formed in the regime of night work, even though the velocities of flow are similar;

- a significantly higher pressure prevails in the steam pipeline in a daily regime, so the flow is tighter and therefore reduces the potential for creating a vortex structures.

References

[1] Badur J.: *Numerical modeling of sustainable combustion in gas turbine.* IMP PAN Publishers, Gdańsk 2003 (in Polish).

[2] Brauschke D., Wiklund D., Kitzman A., Zulic D.: *Thermowell calculations.* Emerson Process Management, White Paper 00840–0200–2654, Rev AC, March 2014.

[3] Goujon-Durand S., Jenffer P., Wesfreid J.E.: *Downstream evolution of the Benard-von Kármán instability.* Phys. Rev. E. **50**(1994), 1.

[4] Klotz L., Goujon–Durand S., Rokicki J., Wesfreid J.E.: *Experimental investigation of flow behind a cube for moderate Reynolds numbers.* J. Fluid Mech. **750**(2014), 73–98.

[5] Saha A.K.: *Three-dimensional numerical study of flow and heat transfer from a cube placed in a uniform flow.* Int. J. Heat Fluid Fl. **26**(2006), 80–94.

[6] Skarysz M., Pryśko J., Goujon–Durand S., Wesfreid J.E.: *The wake behind a rotating sphere.* J. Phys. Conf. Ser. **530**(2014), 012043.

[7] Sarpkaya T.: *A critical review of the intrinsic nature of vortex-induced vibrations.* J. Fluid Struct. **19**(2004), 389–447.

[8] Zarruk G.A, Cowen E.A., Wu T.R., Liu P.L.-F.: *Vortex shedding and evolution induced by a solitary wave propagating over a submerged cylindrical structure.* J. Fluid Struct. **52**(2015), 181–198.

[9] Baarholm G.S, Larsen C.M, Lie H. : *On fatigue damage accumulation from in-line and cross-flow vortex-induced vibrations on risers.* J. Fluid . Struc. **22**(2006), 109–127.

[10] Sakai T., Iwata K., Morishita M., and Kitamura S.: *Vortex-Induced Vibration of a Circular Cylinder in Super-Critical Reynolds number flow and its suppression by structure damping.* JSME Int. J. Ser. B **44**(2001), 712–720.

[11] Jiang Y.Y., Yoshimura S., Imai R., Katsura H., Yoshida T., Kato C.: *Quantitative evaluation of flow-induced structural vibration and noise in turbomachinery by full-scale weakly coupled simulation.* J. Fluids Struct. **23**(2007), 531–544.

[12] Thapa B.S., Thapa B., Dahlhaug O.G.: *Current research in hydraulic turbines for handling sediments.* Energy **47**(2012), 62–69.

[13] Lee A.H., Campbell R.L., Hambric S.A.: *Coupled delayed-detached-eddy simulation and structural vibration of a self-oscillating cylinder due to vortex-shedding.* J. Fluids Struct. **48**(2014), 216–234.

[14] Deng J., Shao X-M., Fu X., Zheng Y.: *Evaluation of the viscous heating induced jam fault of valve spool by fluid-structure coupled simulations.* Energ. Convers. Manage. **50**(2009), 947–954.

[15] Chrust M., Goujon-Duran S., Wesfreid J.E.: *Loss of a fixed plane of symmetry in the wake of a sphere.* J. Fluids. Struct. **41**(2013), 51–56.

[16] Gumowski K., Miedzik J., Goujon-Duran S., Jenffer P., Wesfreid J.E.:
     *Transition to a time-dependent state of fluid flow in the wake of a
     sphere.* Phys. Rev. E **77**(2008), 055308(R).

[17] Norberg C.: *Fluctuating lift on a circular cylinder: review and new
     measurements.* J. Fluid Struct. **17** (2003), 57–96.

[18] Kulińczak A, Pankanin G.: *Modeling Von Kármán vortex path using
     Ansys Fluent package* . Przegląd elektrotechniczny **90**(2014), 8 (in Pol-
     ish).

[19] Badur J.: *Development of energy concept.* IMP PAN Publishers,
     Gdańsk 2009 (in Polish).

[20] Shyy W.: *Computational Modeling for Fluid Flow and Interfacial
     Transport.* Dover Pub., NY 1994.

[21] Prandtl L: *Flow Dynamics.* PWN, Warsaw 1956 (in Polish).

[22] Jou D., Casas-Vazquez J., Criado-Sancho M.: *Thermodynamics of
     Fluid under Flow.* Springer, Berlin 2001.

[23] Fuchs R., Hopff L., Seewald F.: *Aerodynamik.* Springer, Berlin 1934.

[24] Prosnak W.J.: *Fluid Mechanics.* PWN, Warsaw 1970 (in Polish).

[25] Szaltys P., Chrust M., Przadka A., Goujon-Duran S., Tuckerman L.S.,
     Wesfreid J.E.: *Nonlinear evolution of instabilities behind spheres and
     disks.* J. Fluids Struct. **28**(2012), 483–487.

[26] Badur J., Karcz M., Lemański M., Nastałek L.: *Foundations of the
     Navier-Stokes boundary conditions in fluid mechanics.* Transactions
     IFFM **123**(2011), 3–55.

[27] Ziółkowski P., Badur J.: *Navier number and transition to turbulence.*
     J. Phys.: Conf. Ser. **530**(2014), 012035.

[28] Pietraszkiewicz W., Konopińska V.: *Singular curves in the resultant
     thermomechanics of shell.* Int. J. Eng. Sci. **80**(2014), 21–31.

[29] Badur J., Charun H.: *Selected problems of heat exchange modelling in
     pipe channels with ball turbulisers.* Arch. Thermodyn. **28**(2007), 65–88.

[30] Laudner B.E., Spalding D.B.: *The numerical computation of turbulent
     flows.* Comput. Method. Appl. M. **3**(1974), 2, 269–289.

[31] Badur J.: *Five Lectures of Contemporary Fluid Thermomechanical Flu-
     ids.* 2nd Edn., IMP PAN Publishers, Gdańsk 2005 (in Polish).

[32] Gawroński W.: *Advanced Structural Dynamics and Active Control of Structures.* Springer, 2004.

[33] Zienkiewicz O.C.: *Finite Element Method.* Vol. I,II, and III. Elsevier, 2005.

[34] Calderer R., Masud A.: *A multiscale stabilized ALE formulation for incompressible flows with movieng boundaries.* Comp. Mech **46**(2010), 185–197.

[35] Czechowicz K., Badur J., Narkiewicz K.: *Two-way FSI modelling of blood flow through CCA accounting on-line medical diagnostics in hypertension.* J. Phys.: Conf. Ser. **530**(2014), 012011.

[36] Kaliński K.J.: *Chatter vibration surveillance by the optimal linear spindle speed control.* Mech. Sys. Signal Proces. **25**(2011), 383–399.

[37] Sławiński D.: *A novel shake-down adaptation concept for the modern starts-ups of steam turbines.* PhD thesis, The Szewalski Institute of Fluid–Flow Machinery PASci, Gdańsk 2015 (in Polish).

[38] Ziółkowski P.: *The accuracy of the calculation of stress, deformation, vibration frequency and angle of twist single rotor blade depending on the discretization CSD.* In: Modern Technologies and Energy Conversion, (J. Szantyr Ed.), Gdańsk 2011, 185-190 (in Polish).

[39] Badur J., Ziółkowski P., Zakrzewski W., Sławiński D., Kornet S., Kowalczyk T., Hernet J., Piotrowski R., Felicjancik J., Ziółkowski P.J.: *An advanced Thermal-FSI approach to flow heating/cooling.* J. Phys. Conf. Ser. **530**(2014), 10.1088/1742–6596/530/1/012039.

[40] Dettmer W.G., Perić D.: *On the coupling between fluid flow and mesh motion in the modeling of fluid-structure interaction.* Comp. Mech. **43**(2008), 81–90.

[41] Navier CLHM.: *Mémoire sur les lois du mouvement des fluids – presented in Mémoires l'Acad.* Royale des Sciences de l'Institut de France **2**(1822), 375–393.

[42] Brenner H.: *Navier–Stokes revised.* Physica A **349**(2005), 60–132.

[43] Boussinesq J.: *Essai sur la théorie des eaux courantes.* Mémoires l'Académie des Sciences, T. 23 et 24, 1877.

[44] Ziółkowski P., Badur J.: *On the Boussinnesq eddy viscosity concept based on the Navier and du Buat number.* Applied Mechanics 2014 Scientic Session, Book of Abstracts (J. Sawicki Ed.), 87–88.